Title

- **Broad-spectrum immune suppression encoded in self-amplifying RNA enables sustained, reversible, and non-immunostimulatory expression**
- Short title: Non-immunostimulatory, sustained, reversible saRNA

Authors

Tony K.Y. Lim,[1*] Anne Ritoux,[1] Luke W. Paine,[1] Larissa Ferguson,[2] Tawab Abdul,[1] Ewan St. John Smith[1*]

Affiliations

1. Department of Pharmacology, University of Cambridge, Cambridge, UK.

2. MRC Laboratory of Molecular Biology, Cambridge, UK.

* Corresponding authors: TKL: tony.ky.lim@gmail.com, EStJS: es336@cam.ac.uk

Abstract

Self-amplifying RNA (saRNA) triggers ongoing innate immune activation, leading to suppression of cap-dependent translation, cellular mRNA degradation, apoptosis, and proinflammatory cytokine release. As a result, despite the potential for prolonged transgene expression, therapeutic applications of saRNA are largely limited to contexts that benefit from immune activation, such as vaccines. To address this limitation, we developed a fully saRNA-based strategy that simultaneously inhibits multiple dsRNA sensing and inflammatory signaling pathways using cap-independent translation. In mouse primary fibroblast-like synoviocytes—a model relevant to inflammatory joint diseases—this approach reduced cytotoxicity and antiviral cytokine secretion while enabling sustained transgene expression that can be reversed with a small-molecule antiviral. These findings pave the way for saRNA therapies that offer durable, controllable transgene expression without persistent immune activation.

Teaser

A fully self-amplifying RNA-based approach for non-immunostimulatory, sustained, reversible gene expression.

MAIN TEXT

Introduction

Self-amplifying RNA (saRNA), used in two approved vaccines currently in clinical use, demonstrates significant potential in vaccine development (*1*). Upon cellular internalization, saRNA utilizes host machinery to synthesize an RNA-dependent RNA polymerase (RdRp) (*2*). This RdRp generates a negative-strand RNA intermediate, serving as a template for both genomic and subgenomic RNA production (*3*). The subgenomic RNA encodes the gene of interest and is transcribed in excess of the genomic RNA, leading to robust and sustained protein expression (*4*).

While the self-replication of saRNA enables sustained protein expression, it also produces double-stranded RNA (dsRNA) intermediates that activate cytosolic pattern recognition receptors (*5*, *6*). This persistent innate immune activation suppresses cap-dependent

translation (*7–9*), degrades cellular mRNA (*6*, *10*), induces apoptosis (*6*, *11*), and triggers the release of proinflammatory cytokines and chemokines (*12*, *13*). While moderate innate immune stimulation can boost vaccine efficacy (*14*), excessive activation can undermine vaccine potency by reducing antigen expression (*12*). Moreover, this constant activation of the innate immune system impedes the broader applicability of saRNA for non-immunotherapy applications (*15*), necessitating the use of exogenous immunosuppressants to achieve effective transgene expression (*16*).

Strategies to mitigate saRNA-mediated innate immune responses have included the incorporation of modified nucleotides (*17*), and co-delivery of non-replicating mRNA encoding viral innate inhibiting proteins (*18–20*). While these approaches can reduce initial innate immune responses to saRNA transfection, they fall short in addressing the continuous immune activation triggered by dsRNA intermediates that arise during saRNA replication (*2*). Sequence evolution of the RdRp replicon has shown some promise in reducing these responses, but even engineered replicons still induce significant innate immune activation (*6*, *21*). Another strategy involved encoding a viral immune inhibitor within the saRNA construct using a 2A self-cleaving peptide, which improved protein expression in vitro but did not significantly reduce cytokine responses, despite reductions in NF-κB and IRF3 activation (*14*).

Building on previous efforts, we developed a fully saRNA-based approach to mitigate ongoing saRNA-induced innate immune responses. Our strategy incorporates several key innovations. First, innate immune inhibitory proteins are expressed via cap-independent translation, bypassing the cap-dependent translation shutoff commonly triggered by saRNA. Second, by simultaneously targeting multiple dsRNA sensing and inflammatory signaling pathways, our method provides a more comprehensive suppression of innate immune responses than single target approaches. Third, encoding the innate immune inhibitors directly within the saRNA ensures continuous protection against persistent innate immune activation caused by dsRNA intermediates during saRNA replication, eliminating the need for exogenous immunosuppressants.

We evaluated this approach in mouse primary fibroblast-like synoviocytes (FLS), a key cell type in the pathology of inflammatory joint diseases (*22*, *23*). To facilitate this evaluation, we developed a novel microplate assay for straightforward, longitudinal monitoring of saRNA translation control and cytotoxicity in live cells. Our results demonstrate that this strategy effectively reduces saRNA-induced cytotoxicity and cytokine production while enabling sustained cap-dependent transgene expression, which can be reversed with a small-molecule antiviral. These results pave the way for saRNA-based therapies that offer durable, controllable transgene expression with minimal ongoing innate immune activation.

Results

Microplate assay for longitudinal monitoring of translational control and cell viability

Since saRNA can induce cap-dependent translation shutoff and cell death, we developed a microplate assay to simultaneously monitor cap-independent translation, cap-dependent translation, and cell numbers over time in live cells. In this assay, primary mouse FLS (Fig. S1) were plated in 6-well plates and transfected with saRNA constructs designed for dual fluorescence reporting: EGFP was expressed through encephalomyocarditis (EMCV)

internal ribosome entry site (IRES)-mediated, cap-independent translation, while mScarlet3 was expressed through subgenomic cap-dependent translation, allowing assessment of the effects of saRNA on translational control (Fig. 1a). Spectral overlap between EGFP and mScarlet3 was corrected using linear unmixing (Figs. S2a, S2b).

To monitor cell viability, FLS were stained with BioTracker NIR680, a lipid membrane dye that enables longitudinal tracking of cell numbers. Mock transfection using Lipofectamine MessengerMAX increased BioTracker fluorescence compared to non-transfected cells, whereas treatment with the apoptosis inducer staurosporine decreased BioTracker fluorescence, indicating a reduction in cell numbers (Fig. S3a, S3b). The BioTracker results were consistent with those obtained using the viability dye calcein AM (Fig. S3c, S3d), with the added advantages of eliminating the need for additional staining and wash steps and avoiding spectral overlap with red and green fluorescent proteins. This assay allows for seamless longitudinal live cell imaging of cap-independent translation, cap-dependent translation, and cell numbers using microplate readers or laser scanners.

Design of saRNA constructs for inhibiting multiple dsRNA sensing pathways

Cells detect cytosolic dsRNA through various sensing pathways, including RIG-I, melanoma differentiation-associated protein 5 (MDA-5), protein kinase R (PKR), and the oligoadenylate synthase (OAS)/RNase L pathway. To broadly inhibit these pathways, we designed a saRNA construct that uses EMCV IRES cap-independent translation to express the Vaccinia virus E3 protein (Fig. 1a), a pleiotropic inhibitor that binds dsRNA and blocks multiple sensing pathways (*24*). In a second construct, named E3-NSs-L*, we additionally targeted the PKR and OAS/RNase L pathways due to their roles in cap-dependent translational shutoff and cellular mRNA degradation, respectively. In addition to expression of vaccinia virus E3, this construct uses 2A self-cleaving peptides to co-express the Toscana virus NSs protein—an E3 ubiquitin ligase that promotes PKR degradation (*25*)—and Theiler's virus L* protein, which inhibits RNase L (*26*). As a control, we generated a 'native saRNA' construct without inhibitory activity against innate immune pathways, co-expressing a blue fluorescent protein (moxBFP) as a visual marker of IRES functionality.

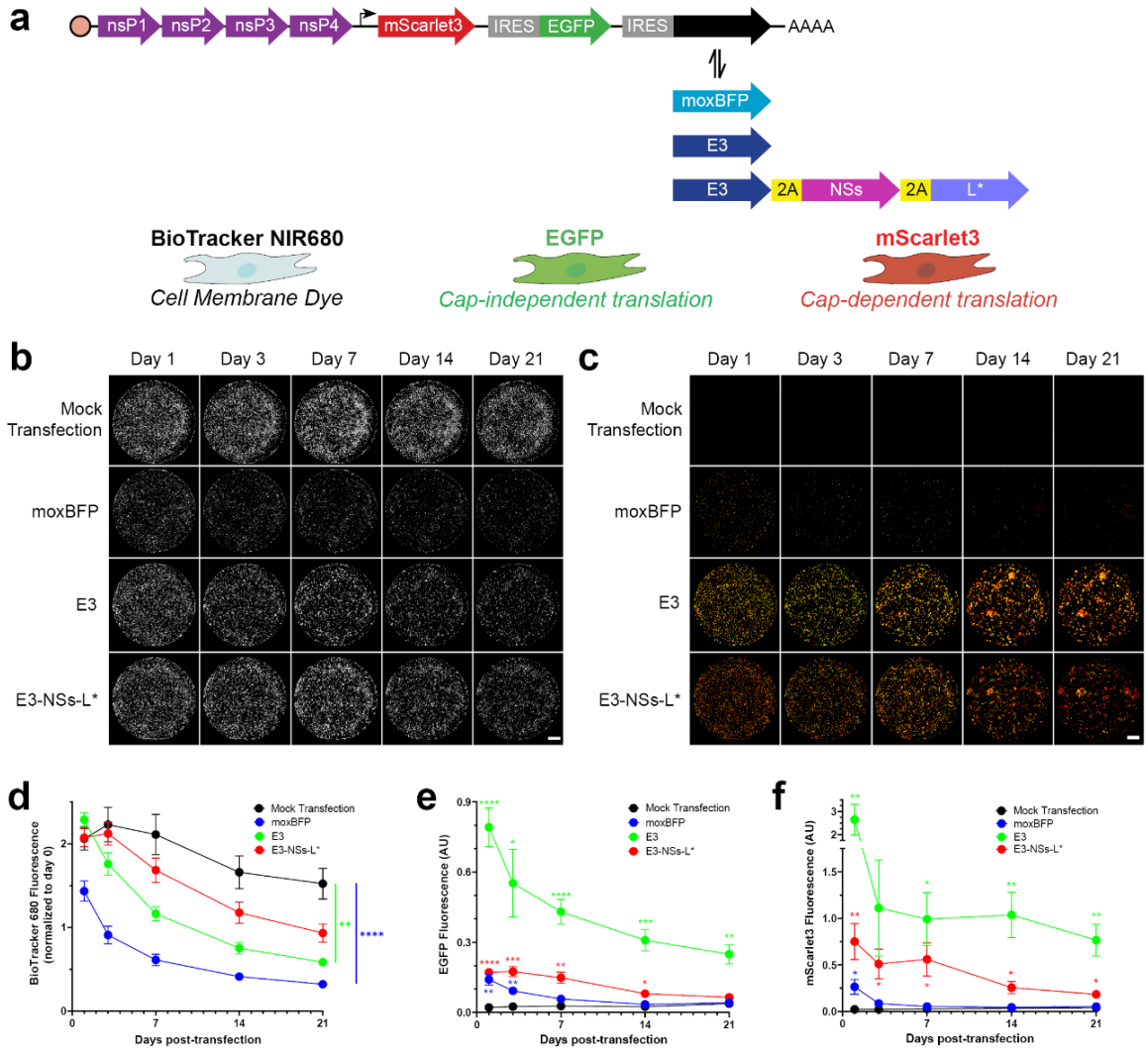

Fig. 1. Cap-independent expression of dsRNA inhibiting proteins reduce cytotoxicity of saRNA and improves cap-dependent transgene expression.

a, Schematic illustrating the different saRNA constructs tested and the *in vitro* reporter assay using primary mouse FLS. The angled arrow signifies the subgenomic promoter.
b, Representative images of BioTracker staining over 3 weeks in FLS transfected with different saRNA constructs. Scale bar = 5 mm.
c, Representative images of EGFP (green) and mScarlet3 (red) expression over 3 weeks in FLS transfected with different saRNA constructs. Scale bar = 5 mm.
d, Quantification of BioTracker fluorescence intensity (n = 11). Statistical significance of main treatment effects compared to mock transfection was determined by two-way RM ANOVA with Dunnett's multiple comparisons test.
e, Quantification of EGFP fluorescence intensity (n = 11). Statistical significance of treatment effects at each time point compared to mock transfection was determined by two-way RM ANOVA with Greenhouse–Geisser correction and Dunnett's multiple comparisons test.
f, Quantification of mScarlet3 fluorescence intensity (n = 11). Statistical significance of treatment effects at each time point compared to mock transfection was determined by two-way RM ANOVA with Greenhouse–Geisser correction and Dunnett's multiple comparisons test.
For all statistical reporting, *P < 0.05, **P < 0.01, ***P < 0.001 and ****P < 0.0001. Data

are presented as mean ± SEM.
nsP, Venezuelan equine encephalitis virus non-structural protein; IRES, encephalomyocarditis virus internal ribosome entry site; moxBFP, monomeric oxidizing environment-optimized blue fluorescent protein; E3, Vaccinia virus E3 protein; NSs, Toscana Virus non-structural NSs protein; L*, Theiler's murine encephalomyelitis virus L* protein; 2A, self-cleaving 2A peptide.

Inhibiting dsRNA sensing reduces cytotoxicity and improves cap-dependent translation

Following transfection of saRNA constructs, we monitored BioTracker, EGFP, and mScarlet3 fluorescence over 3 weeks (Figs. 1b, 1c). Transfection of FLS with native saRNA induced both immediate and long-term cytotoxicity (Fig. 1d). Co-expression of E3 initially preserved cell viability, though it gradually diminished over time. Notably, the E3-NSs-L* construct produced more sustained protection against the decline in cell viability. These findings were corroborated using both the cell number normalization stain CellTag (Fig. S4a) and calcein AM viability dye (Fig. S4b).

Viral innate immune inhibiting proteins significantly enhanced saRNA transgene expression. E3 co-expression produced the highest levels of EGFP and mScarlet3 expression, surpassing both native saRNA and the E3-NSs-L* construct (Figs. 1e, 1f). Native saRNA yielded low transgene levels, while E3-NSs-L* showed intermediate expression. These results indicate that the E3 construct most effectively augments saRNA transgene expression, but at the cost of reduced cell viability.

Apoptosis is a key mechanism of saRNA-induced cytotoxicity

To further investigate the mechanisms underlying saRNA-induced cytotoxicity, a longitudinal apoptosis assay using Annexin-V (A5) staining was conducted. Staurosporine, used as a positive control, caused a temporary increase in A5 staining, which diminished after the cells underwent apoptosis. Native saRNA significantly increased A5 staining in the first two days, while E3 showed a delayed but persistent increase from day 2 onward (Figs. 2a, 2b). In contrast, E3-NSs-L* did not significantly affect A5 staining, indicating reduced cytotoxicity. These patterns aligned with the previously described changes in BioTracker fluorescence (Fig. 1d), cell number normalization stain CellTag (Fig. S4a), and calcein AM viability dye (Fig. S4b).

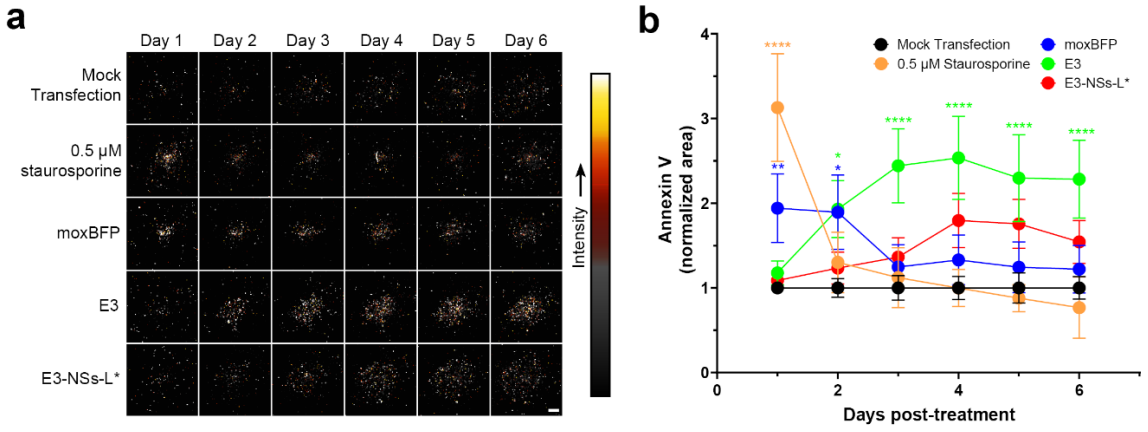

Fig. 2. Inhibiting dsRNA sensing reduces saRNA-induced phosphatidylserine exposure.

a, Representative cropped images of Annexin V-CF800 staining over time in FLS transfected with saRNA constructs shown in Fig. 1a. Scale bar = 1.5 mm.
b, Annexin V signal is presented as the area of positive pixels determined by Li thresholding normalized to the mock transfection group average (n = 6). Statistical significance of treatment effects at each time point compared to mock transfection was determined by two-way RM ANOVA and Bonferonni's multiple comparisons test using one family for all comparisons.
For all statistical reporting, *$P < 0.05$, **$P < 0.01$ ****$P < 0.0001$. Data are presented as mean ± SEM.

Effects of inhibiting dsRNA sensing on translational control

We next explored how the E3 and E3-NSs-L* constructs influence translational control mechanisms during saRNA transfection. In-cell western assays revealed that native saRNA transfection increased eIF2α phosphorylation, but both E3 and E3-NSs-L* effectively blocked this phosphorylation (Fig. 3a), consistent with previous reports of E3's inhibitory effect on eIF2α phosphorylation (*18*). Notably, E3-NSs-L* also increased total eIF2α levels, an effect not observed with the E3 construct (Fig. 3b).

Given that PKR is a key mediator of eIF2α phosphorylation, we further examined PKR levels. As expected from previous reports (*6*), native saRNA transfection elevated PKR levels. Interestingly, co-expression of E3-NSs-L* significantly reduced PKR levels (Fig. 3c), consistent with the role of the Toscana virus NSs protein as an E3 ubiquitin ligase that targets PKR for degradation (*25*).

We also examined the impact on eIF4E, another key factor in translational regulation (*27*). Native saRNA transfection induced eIF4E dephosphorylation without affecting its total levels (Figs. 3d, 3e). Co-expression with either E3 or E3-NSs-L* did not alter these changes in eIF4E phosphorylation or its total levels.

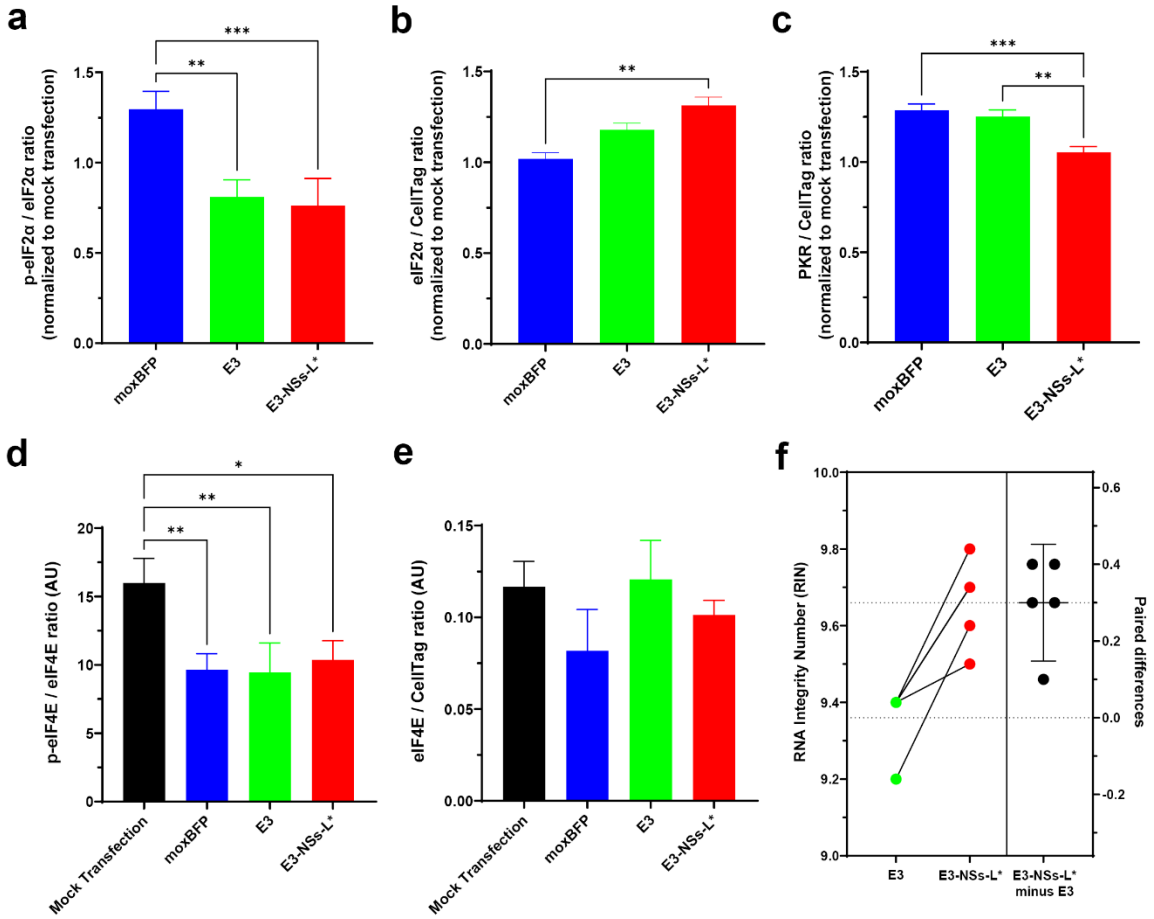

Fig. 3. Impact of dsRNA sensing inhibition on saRNA-induced changes in translational control.

a, In-cell western analysis of phosphorylated eIF2α levels presented as fold-change over mock transfected cells (n = 5). Statistical significance was determined by one-way RM ANOVA and Tukey's multiple comparisons test.
b, In-cell western assay of total eIF2α levels presented as fold-change over mock transfected cells (n = 5). Statistical significance was determined by one-way RM ANOVA and Tukey's multiple comparisons test.
c, In-cell western analysis of PKR levels presented as fold-change over mock transfected cells (n = 4). Statistical significance was determined by one-way RM ANOVA and Tukey's multiple comparisons test.
d, In-cell western analysis of phosphorylated eIF4E levels (n=6). Statistical significance was determined by one-way RM ANOVA and Tukey's multiple comparisons test.
e, In-cell western assay of total eIF4E levels (n = 6). One-way RM ANOVA revealed no significant differences between groups. $F(3,15) = 1.207$, $P=0.3410$.
f, Gardner-Altman comparison plot identifying the difference in RNA integrity number between E3 and E3-NSs-L* constructs after 1 day of transfection (n = 5). The right plot shows mean effect size ± 95% CI. Paired t test, $P = 0.0054$.
saRNA constructs used are shown in Fig. 1a. Statistical significance is indicated as follows: $*P < 0.05$, $**P < 0.01$, and $***P < 0.001$. Unless specified otherwise, data are presented as mean ± SEM.

226 Although the E3-NSs-L* construct both prevents saRNA-induced eIF2α phosphorylation
227 (Fig. 3a) and increases total eIF2α availability for cap-dependent translation initiation
228 (Fig. 3b), it paradoxically resulted in lower mScarlet3 expression compared to the E3
229 construct (Fig. 1f). The E3 construct also generated exceptionally high levels of EGFP
230 expression (Fig. 1e), which was unexpected given that eIF2α phosphorylation was not
231 observed with this construct. Since the Vaccinia virus E3 protein prevents eIF2α
232 phosphorylation and cap-dependent translation shutoff (*18*), this likely promotes robust
233 saRNA replication, leading to the formation of dsRNA intermediates that activate the
234 OAS/RNase L pathway. Activation of RNase L results in the degradation of cellular
235 mRNA, potentially freeing up ribosomes for enhanced saRNA translation—a process that
236 is blocked by Theiler's virus L*, which inhibits RNase L (*26*).

237 Supporting this hypothesis, cells transfected with E3-NSs-L* showed higher RNA
238 integrity than those transfected with the E3 construct (Fig. 3f). The inhibition of RNase L
239 by Theiler's virus L* also explains the reduced cytotoxicity and apoptosis observed with
240 the E3-NSs-L* construct compared to E3 (Figs. 1d, 2b).

241 **Design of saRNA constructs for inhibiting multiple inflammatory signalling**
242 **pathways**

243 Having mitigated saRNA-induced toxicities such as translational shutoff, RNA
244 degradation, and apoptosis, we next focused on addressing saRNA-induced cytokine
245 production. We created constructs expressing E3-NSs-L*-EGFP via one EMCV IRES,
246 and either moxBFP or cellular inhibitors of inflammatory signaling via another EMCV
247 IRES (Fig. 4a). Given that activation of nuclear factor-κB (NF-κB) is a hallmark of viral
248 infection and a master regulator of pro-inflammatory cytokine and chemokine induction
249 (*28*, *29*), we targeted its inhibition using super repressor inhibitor of κBα (srIκBα). This
250 dominant active form of IκBα cannot be phosphorylated and thus resists ubiquitination
251 and degradation, forming a stable cytoplasmic pool that prevents NF-κB nuclear
252 translocation (*30*, *31*). We generated a construct expressing srIκBα alone, and another
253 expressing srIκBα in combination with Smad7 and suppressor of cytokine signaling
254 (SOCS1). Smad7 negatively regulates both transforming growth factor-β (TGF-β) and
255 NF-κB signaling pathways (*32*), while SOCS1 inhibits type I, II and III interferon
256 pathways in addition to NF-κB signaling (*33–35*).

257 **srIκBα co-expression suppresses saRNA-induced cytokine secretion**

258 Using a bead-based immunoassay on FLS culture supernatants, we observed that native
259 saRNA transfection induced cytokine secretion associated with antiviral responses (Fig.
260 4b). Vaccinia virus E3 protein co-expression reduced tumor necrosis factor (TNF)-α,
261 interferon (IFN)-α, and IFN-β levels, while E3-NSs-L* co-expression further decreased
262 CXCL10 levels. Notably, srIκBα co-expression broadly suppressed cytokine secretion,
263 reducing all measured cytokine levels to levels statistically indistinguishable from mock-
264 transfected FLS. The srIκBα-Smad7-SOCS1 construct showed no additional cytokine
265 suppression beyond that achieved by srIκBα alone.

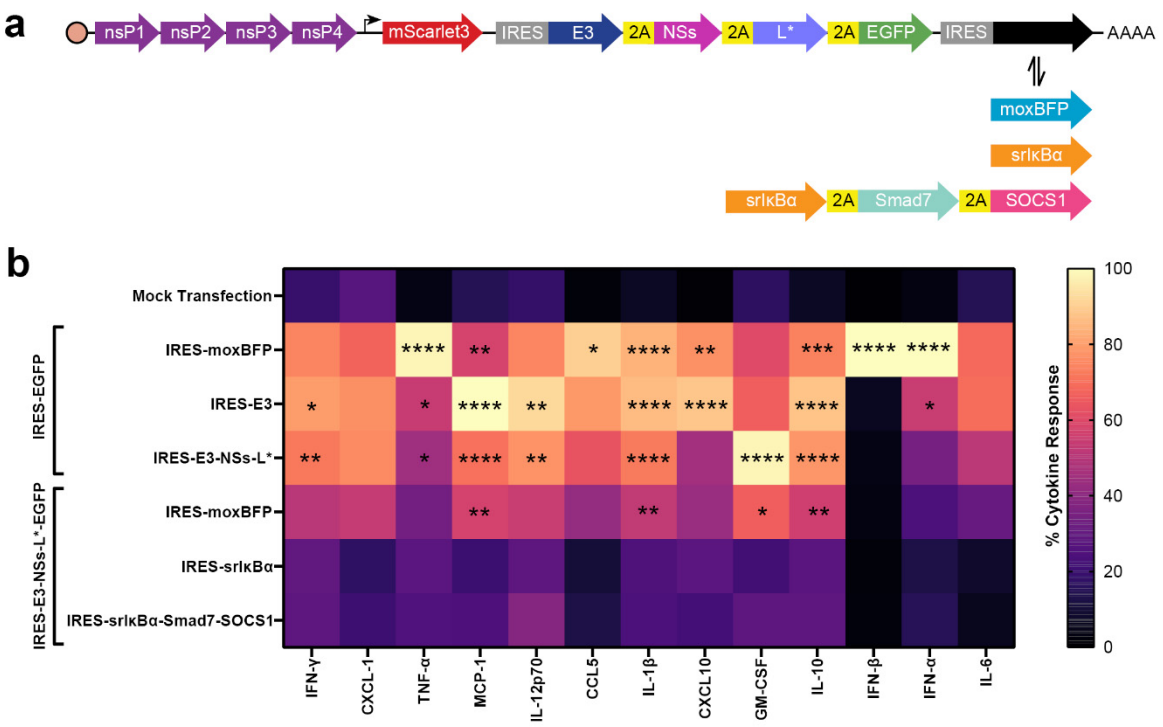

Fig. 4. Cap-independent expression of cellular inhibitors of inflammatory signaling reduce cytokine secretion.

a, Schematic of saRNA constructs designed for inhibition of inflammatory signaling. **b,** Levels of anti-viral cytokines in FLS supernatant collected 2 days post-transfection (n = 6). Statistical significance for each cytokine was assessed using one-way ANOVA followed by Bonferroni's multiple comparisons test against the mock transfection control, with a subsequent Bonferroni correction applied to P values to account for multiple independent hypothesis testing. *$P < 0.05$, **$P < 0.01$, ***$P < 0.001$ and ****$P < 0.0001$. For visualization, cytokine levels were scaled within each biological replicate, with the highest value set to 100%, and the mean values displayed on the heatmap. srIκBα, super-repressor inhibitor of κBα; smad7, mothers against decapentaplegic homolog 7; SOCS1, suppressor of cytokine signaling 1.

srIκBα-Smad7-SOCS1 preserves cell viability and enhances transgene expression

We then examined the impact of inhibiting inflammatory signaling on cell viability and transgene expression (Figs. 5a, 5b). Notably, the srIκBα construct led to reduced cell viability, while the srIκBα-Smad7-SOCS1 construct exhibited a viability profile similar to mock transfection (Fig. 5c). CellTag and calcein AM staining further confirmed the detrimental effects of srIκBα on cell viability (Figs. S5a, S5b). All three constructs produced low levels of EGFP expression post-transfection (Fig. 5d), as expected given EGFP's position as the fourth protein in a quad-cistronic 2A element (Fig. 4a). Previous studies have shown that expression levels decrease significantly for proteins located later in quad-cistronic 2A arrangements (*36*). Interestingly, while the moxBFP and srIκBα constructs yielded relatively low mScarlet3 levels, the srIκBα-Smad7-SOCS1 construct demonstrated 2- to 4-fold higher mScarlet3 fluorescence compared to the others (Fig. 5e).

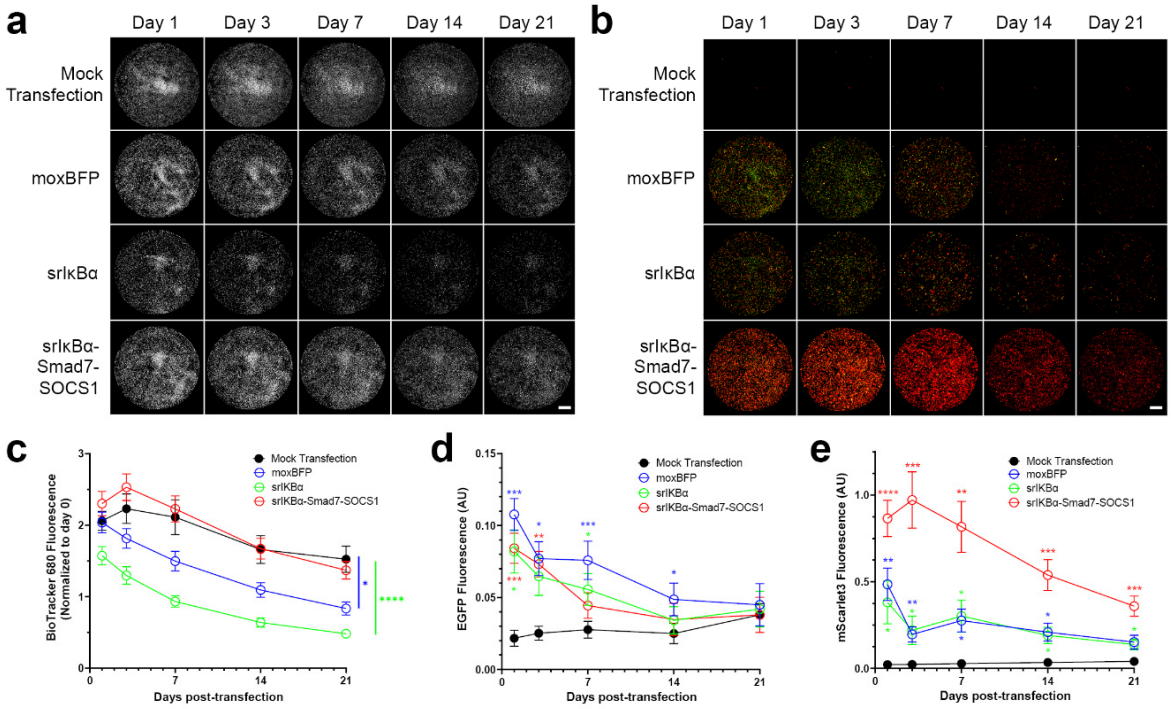

Fig. 5. Differential effects of srIκBα and srIκBα-Smad7-SOCS1 on cell viability and transgene expression.

a, Representative images of BioTracker staining over 3 weeks in FLS transfected with different saRNA constructs. Scale bar = 5 mm.
b, Representative images of EGFP (green) and mScarlet3 (red) expression over 3 weeks in FLS transfected with different saRNA constructs. Scale bar = 5 mm.
c, Quantification of BioTracker fluorescence intensity (n = 11). Statistical significance of main treatment effects compared to mock transfection was determined by two-way RM ANOVA with Dunnett's multiple comparisons test.
d, Quantification of EGFP fluorescence intensity (n = 11). Statistical significance of treatment effects at each time point compared to mock transfection was determined by two-way RM ANOVA with Greenhouse–Geisser correction and Dunnett's multiple comparisons test.
e, Quantification of mScarlet3 fluorescence intensity (n = 11). Statistical significance of treatment effects at each time point compared to mock transfection was determined by two-way RM ANOVA with Greenhouse–Geisser correction and Dunnett's multiple comparisons test.
saRNA constructs used are shown in Fig. 4a. For all statistical reporting, *$P < 0.05$, **$P < 0.01$, ***$P < 0.001$ and ****$P < 0.0001$. Data are presented as mean ± SEM.

srIκBα-mediated eIF4E depletion contributes to reduced transgene expression

Interestingly, co-expression of srIκBα resulted in eIF2α dephosphorylation, an effect not seen with the srIκBα-Smad7-SOCS1 construct (Fig. 6a). Neither construct affected total eIF2α levels or eIF4E phosphorylation (Figs. 6b, 6c), but srIκBα reduced total eIF4E levels, whereas srIκBα-Smad7-SOCS1 did not (Fig. 6d). As a low-abundance initiation factor essential for synthesizing nearly all cellular proteins, eIF4E plays a critical role in regulating cap-dependent translation (*37*). Therefore, in addition to decreased cell

viability, the srIκBα-induced reduction in eIF4E likely contributes to the lower transgene expression observed with the srIκBα construct.

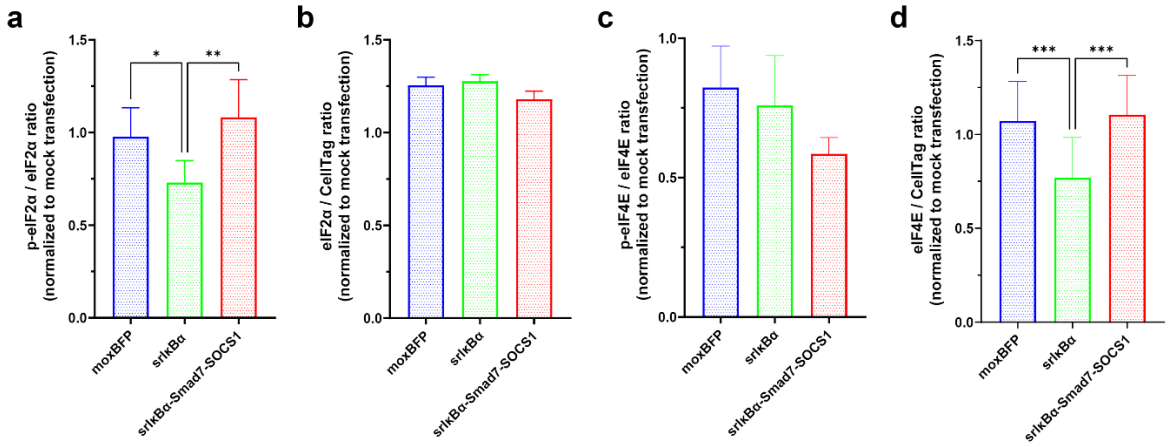

Fig. 6. Impact of srIκBα and srIκBα-Smad7-SOCS1 on translational control.

a, In-cell western analysis of phosphorylated eIF2α levels presented as fold-change over mock transfected cells (n = 6). Statistical significance was determined by one-way RM ANOVA and Holm-Šídák's multiple comparisons test to compare all groups.
b, In-cell western analysis of total eIF2α levels presented as fold-change over mock transfected cells (n = 6). One-way RM ANOVA revealed no significant difference between groups. $F(2,8)=3.683$, $P=0.0735$.
c, In-cell western analysis of phosphorylated eIF4E levels presented as fold-change over mock transfected cells (n = 6). One-way RM ANOVA revealed no significant difference between groups. $F(2,10)=1.336$, $P=0.3059$.
d, In-cell western analysis of total eIF4E levels presented as fold-change over mock transfected cells (n=6). Statistical significance was determined by one-way RM ANOVA and Holm-Šídák's multiple comparisons test to compare all groups.
saRNA constructs used are shown in Fig. 4a. For all statistical reporting, $*P < 0.05$, $**P < 0.01$ and $***P < 0.001$. Data are presented as mean ± SEM.

Reversibility of saRNA transfection using a small-molecule antiviral

Next, we evaluated the reversibility of srIκBα-Smad7-SOCS1 saRNA transfection. ML336 (*38*), a small-molecule inhibitor of the VEEV RdRp used in this study, was added to the culture medium 1 day after transfection (Fig. 7a). ML336 treatment significantly reduced EGFP and mScarlet3 expression after several days (Figs. 7b, 7c), demonstrating its effectiveness in inhibiting saRNA transfection. Notably, ML336 did not reduce cell viability, as shown by calcein AM staining, when compared to vehicle or mock transfection (Fig. 7d).

Prolonged srIκBα-Smad7-SOCS1 transfection reduces basal fibroblast activation factor-α levels

Given that viral infection is known to drive inflammatory fibroblast activation (*39*, *40*), we investigated whether prolonged saRNA transfection could have a similar effect on FLS. We examined fibroblast activation factor-α (FAP-α), a protein involved in joint destruction that is typically expressed at low basal levels in FLS but upregulated upon

inflammatory activation (*41–43*). Notably, FAP-α levels at day 11 post-transfection were lower than mock transfection and significantly reduced by srIκBα-Smad7-SOCS1 co-expression (Fig. 7e). These findings suggest that long-term saRNA transfection with the srIκBα-Smad7-SOCS1 construct not only avoids activating FLS but may also serve as an effective strategy to downregulate FAP-α expression, which could be advantageous in arthritis therapy (*44*).

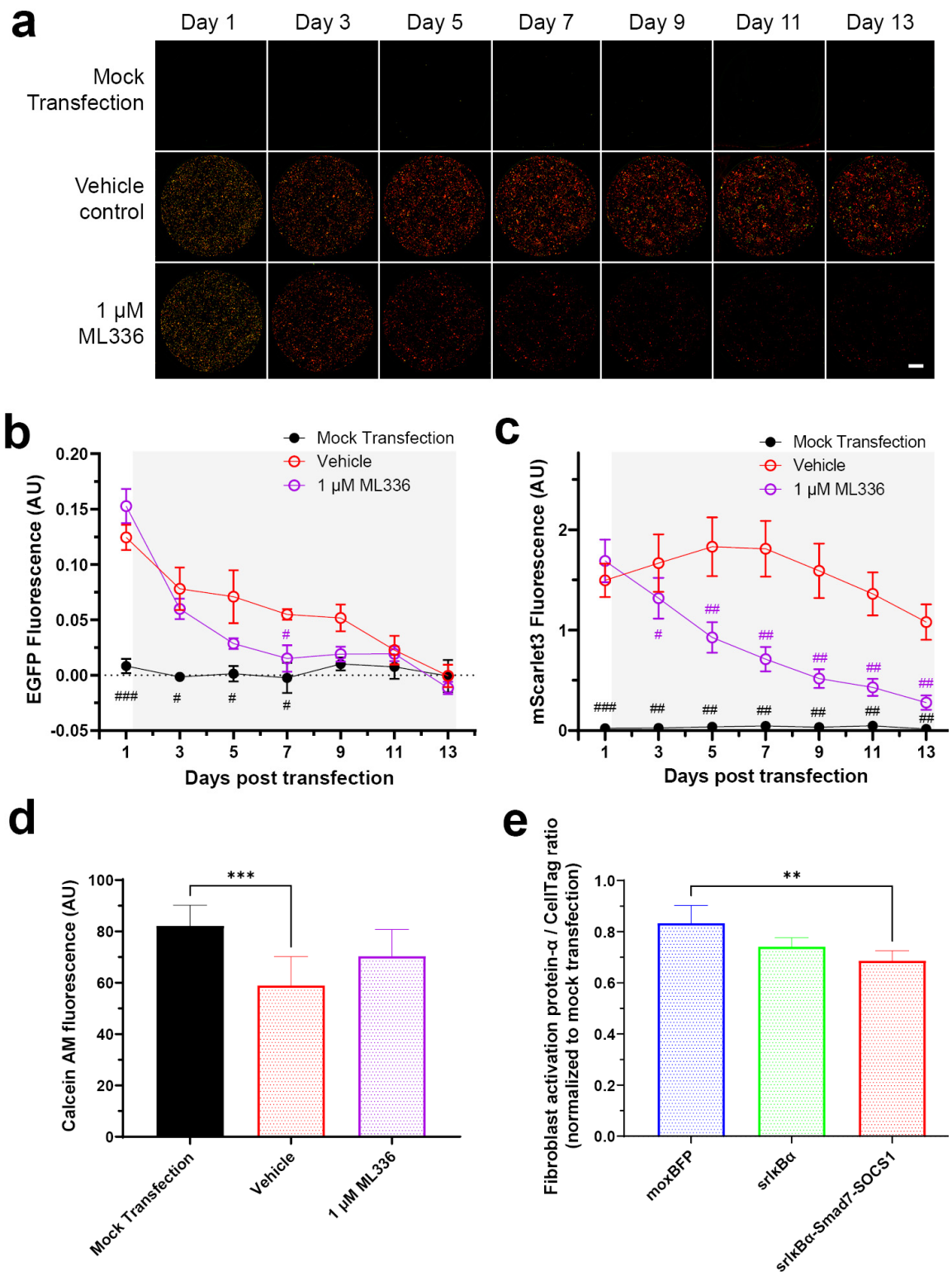

Fig. 7 Reversibility of srIκBα-Smad7-SOCS1 saRNA transfection and its effects on fibroblast activation factor-α expression

a, Representative images of EGFP (green) and mScarlet3 (red) expression over 3 weeks in FLS transfected with the construct encoding srIκBα-smad7-SOCS1. Cultures were treated with vehicle or 1 μM ML336. Scale bar = 5 mm.
b, Quantification of EGFP fluorescence intensity in FLS cultures transfected with the construct encoding srIκBα-smad7-SOCS1 and treated with 1 μM ML336 or vehicle (n = 6). Shading represents the treatment time course, starting 1 day post-transfection. Statistical significance compared to the vehicle treated condition was determined by two-way RM ANOVA with Greenhouse–Geisser correction and Dunnett's multiple comparisons test. # P<0.05 and ###P<0.01.
c, Quantification of mScarlet3 fluorescence intensity in FLS cultures transfected with the construct encoding srIκBα-smad7-SOCS1 and treated with 1 μM ML336 or vehicle (n = 6). Shading represents the treatment time course, starting 1 day post-transfection. Statistical significance compared to the vehicle treated condition was determined by two-way RM ANOVA with Greenhouse–Geisser correction and Dunnett's multiple comparisons test. # P<0.05, ##P<0.01, and ###P<0.01.
d, Quantification of calcein AM staining after 12 days of vehicle or ML336 treatment (day 13 post-transfection, n = 6). Statistical significance was determined by one-way RM ANOVA and Bonferroni's multiple comparison's test to compare all groups. ***P<0.001.
e, In-cell western analysis of fibroblast activation protein-α levels after 11 days of transfection presented as fold-change over mock transfected cells (n = 8). saRNA constructs are shown in Fig. 4a. Statistical significance was determined by one-way RM ANOVA and Tukey's multiple comparisons test. **P<0.01.
Data are presented as mean ± SEM.

Discussion

Preclinical and clinical data show that saRNA vaccines typically trigger an intense innate immune response that can inhibit antigen expression (*8*, *13*, *18*). While a degree of innate immune activation can enhance immunogenicity, saRNA often provokes excessive immunostimulation, which limits antigen expression and necessitates strategies to mitigate this response (*15*). Additionally, saRNA vaccines can induce significant inflammation (*45*, *46*), which is increasingly recognized as problematic, as common adverse events include pain, headache, tenderness, arthralgia, fever, and chills (*47*, *48*). Potentially, the approach described in this study, which dampens multiple innate immune pathways, could be applied in future saRNA vaccine designs to both improve antigen expression and reduce reactogenicity.

Most studies have focused on reducing early innate immune responses to saRNA while maximizing transgene expression (*9*, *17*, *18*). However, our findings suggest that extremely high levels of saRNA transgene expression may be indicative of saRNA-induced toxicities such as cellular mRNA degradation. This was evident in the saRNA construct encoding only Vaccinia virus E3, without additional innate immune inhibitors. Although this saRNA construct did not immediately affect cell viability, long-term viability was reduced. Therefore, it may be well-suited for vaccine applications, where maximizing antigen expression outweighs concerns about long-term cell viability. In contrast, for non-immunotherapy applications, maintaining long-term cell viability is likely more critical than achieving extremely high levels of transgene expression.

Long-term cytotoxicity induced by saRNA is associated with the persistent activation of cytosolic dsRNA sensors. Our findings support this hypothesis, showing that targeting additional dsRNA sensing pathways with viral immune inhibitors can reduce saRNA-induced cytotoxicity. Alphavirus replicons, such as the VEEV replicon used in this study, replicate within plasma membrane invaginations called spherules—structures that partially shield dsRNA intermediates from cytosolic detection (*3*). However, this shielding is not complete, as alphavirus replicons still activate cytosolic dsRNA sensors PKR, RIG-I, and MDA-5 (*5*, *7*, *18*) , leading to continuous type I interferon release (*49*). This sustained interferon production restricts saRNA transgene expression; for instance, in a study using saRNA for in situ therapeutic antibody production, an interferon-α/β receptor-1 blocking antibody had to be administered before virus challenge to achieve protective antibody levels (*16*). To fully unlock the potential of the saRNA platform for sustained transgene expression in non-immunotherapy applications, it is crucial to mitigate this persistent activation of the innate immune response.

In this study, we demonstrate that persistent saRNA-induced innate immune activation can be suppressed by engineering saRNA to express a combination of dsRNA sensing and inflammatory signaling inhibitors using cap-independent translation. saRNA replication activates PKR, leading to eIF2α phosphorylation and suppression of cap-dependent translation (*7*, *18*). This suppression frees host ribosomes for IRES-mediated cap-independent translation (*50*). As a result, cap-independent expression of inhibitors ensures that their levels increase as translation suppression intensifies, effectively countering the innate immune response. In contrast, cap-dependent expression of inhibitors would lead to decreased levels during translation suppression, making it a less reliable strategy for mitigating the innate immune activation triggered by saRNA.

We found that saRNA induces eIF4E dephosphorylation, a phenomenon previously observed in alphavirus replicons, though the underlying mechanism remains unclear (*51*, *52*). Like eIF2α phosphorylation, eIF4E dephosphorylation reduces cap-dependent saRNA transgene expression and global translation while boosting cap-independent transgene expression (*53*). These combined effects—eIF2α phosphorylation and eIF4E dephosphorylation—explain why IRES-driven, cap-independent transgenes achieve higher expression compared to those relying on cap-dependent translation when using native saRNA (*16*, *54*).

Additionally, we found that srIκBα expression decreased eIF4E levels, consistent with previous findings (*55*). The ability of saRNA or srIκBα expression to lower eIF4E activity could have therapeutic value, as reduced eIF4E activity has been associated with decreased pain sensitivity (*56*), inhibition of tumorigenesis (*57*), improvement of neurodevelopmental social deficits (*58*), and increased longevity (*59*). We also observed that srIκBα expression induced eIF2α dephosphorylation, while the E3-NSs-L* construct reduced PKR levels. Since eIF2α phosphorylation activates the integrated stress response (ISR)— a pathway often driven by PKR in age-related diseases like neurodegeneration (*60*)—saRNA may represent a novel approach to modulate the ISR in these conditions.

The NF-κB pathway is a key regulator of pro-inflammatory cytokine production, making it an important target for suppressing inflammatory signaling (*61*). However, NF-κB also has pro-survival functions as it promotes the transcription of anti-apoptotic genes—though exact effects vary by tissue type and biological context (*62*). In FLS, studies have shown that overexpression of srIκBα effectively reduces inflammatory cytokine production but increases sensitivity to TNF-α-induced apoptosis (*63*, *64*). Our findings are consistent with these observations; saRNA encoding srIκBα decreased both pro-inflammatory cytokine levels and cell viability.

Although inducing apoptosis can be beneficial in some therapeutic settings, it conflicts with the goal of sustained transgene expression. Co-expressing Smad7 and SOCS1 effectively counteracted srIκBα-induced cell death. While we did not assess the individual contributions of each protein, both are known to have anti-apoptotic properties in certain contexts. Smad7 can inhibit TGF-β-induced apoptosis (*65*, *66*), while SOCS1 can suppress apoptosis triggered by IFN-α, IFN-β (*67*), IFN-γ (*68*), and TNF-α (*69–71*). These anti-apoptotic effects likely allow Smad7 and SOCS1 to mitigate srIκBα-induced reductions in cell viability.

Additionally, co-expression of Smad7 and SOCS1 significantly enhanced cap-dependent transgene expression. Although we did not distinguish the contributions of each protein to this effect, it is likely mediated by SOCS1. Previous studies have shown that ruxolitinib, a small-molecule inhibitor of Janus kinase (JAK) 1 and JAK2 (*72*), increases saRNA protein expression when added to saRNA polyplexes (*13*). SOCS1 is an endogenous inhibitor of JAK1 and JAK2 (*73*), therefore, SOCS1 offers a genetically encoded alternative to the small-molecule approach of ruxolitinib for enhancing saRNA expression.

The NF-κB, TGF-β, and JAK/signal transducer and activator of transcription (STAT) pathways are central to the progression of osteoarthritis (*74–76*). The srIκBα-Smad7-SOCS1 saRNA construct provides a novel strategy to simultaneously target these pathways: srIκBα inhibits NF-κB, Smad7 blocks TGF-β, and SOCS1 suppresses the JAK/STAT pathway. Each of these proteins has been independently studied as a treatment for osteoarthritis (*77–79*), and combining them into a single construct could enhance therapeutic efficacy, meriting further exploration in disease models. The approach in this study also underscores the versatility of the saRNA platform, which can efficiently integrate multiple transgenes and genetic elements. Our largest construct included the VEEV RdRP, two IRES sequences, five 2A peptides, and eight transgenes within a 16.5-kilobase saRNA. This ability to encode numerous transgenes without apparent size constraints is a notable yet underutilized strength of the saRNA platform.

Furthermore, this study presents a straightforward method for controlling saRNA activity. ML336, a VEEV RdRp inhibitor, blocks the synthesis of positive-sense genomic, negative-sense template, and subgenomic RNAs of VEEV without affecting host cellular RNA transcription (*80*). It has an in vitro effective concentration 50 (EC_{50}) of 0.02-0.04 μM, and a 50 mg/kg dose offers 100% protection in a lethal VEEV mouse infection model, with no observed toxicity (*81*). Thus, ML336 and other RdRp inhibitors provide a practical means to deactivate saRNA—either to terminate transgene expression once therapeutic objectives are met or as a safety measure to reduce the risks associated with prolonged innate immune suppression and other potential side effects, including adaptive immune responses to the VEEV replicon.

Our findings introduce a novel fully saRNA-based strategy to overcome a key limitation of saRNA: continuous innate immune stimulation. By inhibiting multiple innate immune pathways through proteins expressed via cap-independent translation, we achieve sustained transgene expression with low cytotoxicity and minimal antiviral cytokine induction, all without the use of exogenous immunosuppressants. This advancement expands the therapeutic applications of saRNA to scenarios where prolonged innate immune activation is undesirable, including protein replacement therapy, therapeutic antibody production, genome editing, cellular reprogramming, and immune cell engineering. Importantly, the reversibility of this approach offers significant advantages, enabling precise control over transgene expression and serving as a crucial safety mechanism for clinical applications.

Materials and Methods

Experimental Design

This study aimed to develop and evaluate saRNA constructs that modulate innate immune responses, specifically targeting dsRNA sensing and inflammatory signaling pathways, to enhance cell viability, reduce cytokine expression, and achieve sustained transgene expression. To this end, we engineered saRNA constructs that co-express multiple viral innate immune inhibitors and cellular inhibitors of inflammatory signaling. The constructs were designed to enable monitoring of cap-dependent and cap-independent translation using distinct fluorescent proteins.

The experimental approach included cloning the saRNA constructs using molecular biology techniques, followed by in vitro transcription and transfection into mouse primary FLS. Transfected cells were analyzed using fluorescence-based microplate assays to assess cell viability, apoptosis, and protein expression over time. Further evaluations of translational control, FLS activation markers, RNA integrity, and cytokine secretion were conducted using in-cell western assays, capillary electrophoresis, and bead-based immunoassays. Finally, the reversibility of saRNA transfection was explored using a small-molecule inhibitor targeting the VEEV RdRp.

Plasmid cloning and construct design

The commercially available TagGFP2 E3L Simplicon vector (SCR725, Merck) served as the saRNA backbone in this study. After removing the TagGFP2-IRES-E3 sequence, various constructs were generated by combining different elements using restriction digests (FastDigest, Thermo Scientific), overlap extension PCR (Phusion, Thermo Scientific), and HiFi assembly (NEBuilder, New England Biolabs).

Genetic elements were sourced as follows: mScarlet3 from pDx_mScarlet3 (a gift from Dorus Gadella [Addgene plasmid #189754]) (*82*), IRES-EGFP from pIRES2-EGFP (Clontech), and IRES-E3 and IRES-PuroR (puromycin resistance) from the original TagGFP2 E3L Simplicon vector.

Custom gene synthesis (GeneArt, Thermo Scientific) was used to produce IRES-moxBFP, IRES-E3-T2A-NSs-P2A-L*-E2A-mEGFP, and IRES-srIκBα-P2A-Smad7-T2A-SOCS1 sequences. The IRES sequence was derived from pIRES2-EGFP (Clontech). Other sequences were derived from public databases: moxBFP (FPbase ID: SSTDU) (*83*), mEGFP (FPbase ID: QKFJN), E3 (UniProt: P21605-1), NSs (UniProt: P21699), L* (UniProt: P0DJX4), Smad7 (UniProt: O35253-1), and SOCS1 (UniProt: O35716). srIκBα was engineered from IκBα (UniProt: Q9Z1E3) by substituting serines 32 and 36 with alanines. All synthesized sequences were codon-optimized for mouse expression (GenSmart, GenScript).

Plasmids were cloned in DH5α competent *Escherichia coli* (High Efficiency, New England Biolabs) and purified by maxiprep (PureLink HiPure, Invitrogen). All plasmid sequences were verified using nanopore whole plasmid sequencing (Plasmidsaurus).

RNA synthesis

Plasmids were linearized using XbaI (FastDigest, Thermo Scientific) at 37°C for 3 hours. The linear plasmids were purified by phenol-chloroform extraction followed by sodium acetate ethanol precipitation. Uncapped RNA was synthesized *in vitro* using the T7 RiboMAX Large Scale RNA Production kit (Promega) at 37°C for 2 hours. After purification by ammonium acetate precipitation, the RNA was denatured at 65°C for 5 minutes. Cap-1 structures were then generated using the Vaccinia Capping System in

551 conjunction with mRNA cap 2'-O-methyltransferase (both from New England Biolabs) for
552 45 minutes at 37°C. Following another ammonium acetate purification, the RNA was
553 treated with Antarctic phosphatase (New England Biolabs) for 30 minutes at 37°C. After a
554 final ammonium acetate purification step, the RNA was resuspended in THE RNA
555 Storage Solution (Invitrogen), aliquoted, and stored at -80°C until use.
556
557 **Animals**
558 All mice used in this study were 5- to 12-week-old wildtype C57BL/6J mice (Bicester,
559 UK). Both male and female mice were included, though sex differences in response to
560 saRNA transfection were not analyzed. Mice were housed in groups of up to five in a
561 temperature-controlled room (21°C), with bedding, a red shelter, and enrichment materials
562 provided. They were maintained on a 12-hour light/dark cycle, with food and water
563 available ad libitum. Mice were euthanized by exposure to CO_2 gas in a rising
564 concentration, and death confirmed by dislocation of the atlanto-occipital joint by
565 applying pressure to the side of the neck using thumb and forefinger, procedures in line
566 with the Animals (Scientific Procedures) Act 1986 Amendment Regulations 2012.
567
568 **Mouse primary FLS culture**
569 We cultured FLS from mouse knee joints following established protocols (*84*), with slight
570 modifications. In brief, knee joints were exposed by cutting through the overlying skin
571 with dissecting scissors. The patellar tendon was then grasped near the patella with
572 Dumont tweezers, and spring scissors were used to sever the patellar tendon along with
573 surrounding tissues. Finally, the patella was excised by cutting the quadriceps tendon, and
574 excess muscle and tendons were carefully trimmed away.
575 Both patellae from each animal were collected into a microcentrifuge tube containing ice-
576 cold sterile phosphate buffered saline (PBS), then transferred to a 24-well tissue culture
577 plate (Costar) with FLS culture media. The media consisted of DMEM/F-12 (Invitrogen)
578 supplemented with 25% fetal bovine serum (Sigma), 1X GlutaMAX (Gibco), and 100
579 µg/ml Primocin (InvivoGen).
580 The patellae were maintained in a humidified incubator at 37°C with 5% CO2, with media
581 changes every 1-2 days. FLS outgrowth was observed, and after approximately 10 days,
582 when cells reached 70% confluency, the patellae were transferred to new wells for further
583 FLS collection. Cells attached to the original wells were passaged using 0.1% trypsin-
584 EDTA (Sigma) into a single well of a 6-well plate (Costar). Cells were later expanded into
585 T25 flasks (BioLite, Thermo Scientific or CELLSTAR, Greiner Bio-One) and passaged
586 upon reaching confluency. After the second passage, Versene solution (Gibco) was used
587 for cell dissociation.
588 FLS were used between passages 3 and 8. In most experiments, cells from the same
589 animal were divided and plated onto 6-well or 24-well plates, allowing for parallel
590 manipulations with matched conditions. Occasionally, when cell numbers were low, cells
591 from different animals were pooled before division. Once plated for experiments, media
592 was changed every 2-3 days.
593
594 **Immunocytochemistry and confocal microscopy**
595 Cells were plated on poly-D-lysine-coated glass-bottom 35 mm dishes (P35GC-1.5-14-C,
596 MatTek) and fixed with 4% paraformaldehyde for 10 minutes at room temperature
597 without permeabilization. After fixation, cells were washed twice with PBS, followed by
598 blocking with 10% normal goat serum in PBS for 1 hour at room temperature.
599 Cells were then incubated overnight at 4°C in blocking buffer, either without primary
600 antibody (no primary control) or with cadherin-11 (extracellular) rabbit polyclonal

antibody (1:200, DF3523, Affinity Biosciences). After three washes with PBS, cells were incubated for 1 hour at room temperature in blocking buffer with 1 µg/ml Hoechst 33342, BioTracker NIR680 (1:2000, Merck), and goat anti-rabbit Alexa Fluor 488 secondary antibody (1:500, Invitrogen).
After four additional PBS washes, cells were imaged in PBS using a Leica Stellaris 5 confocal microscope equipped with a 40X oil immersion objective. Tile-scanned images were stitched using Las X microscopy software (Leica) to generate high-resolution panoramic images.

BioTracker staining
BioTracker NIR680 was diluted 1:2000 in unsupplemented DMEM/F-12. T25 flasks containing FLS were washed once with HBSS (with calcium and magnesium, Gibco), then incubated with the diluted dye for 30 minutes at 37°C. After incubation, the flasks were washed three times with FLS media, with each wash lasting 10 minutes at 37°C. The FLS were then dissociated using Versene and plated onto 6- or 24-well plates.

FLS transfection
For transfection in 6-well plates, the medium was removed and replaced with 1 ml of Opti-MEM I (Gibco). In a microcentrifuge tube, 500 ng of saRNA was diluted in 200 µl of Opti-MEM I. In a separate tube, 3 µl of Lipofectamine MessengerMAX (Invitrogen) was diluted in 100 µl of Opti-MEM I. After gently mixing, the complexes were incubated at room temperature for 5 minutes, then added dropwise to the cells. The cells were incubated with the complexes for 2 hours at 37°C, after which the media was removed and replaced with fresh FLS media. For transfection in 24-well plates, all volumes and amounts of saRNA were reduced fivefold.

Microplate imaging
Unless otherwise specified, black glass-bottom 6-well plates (P06-1.5H-N, Cellvis) were used for microplate imaging. Prior to imaging, the FLS media was replaced with Live Cell Imaging Solution (Invitrogen). Imaging was performed using the Odyssey M laser scanner (LI-COR), using LI-COR acquisition software with a plate offset of +1.45 mm and 100 µm resolution.
EGFP, mScarlet3, and BioTracker NIR680 were imaged using the 488, 520, and 700 channels, respectively. Spectral cross-excitation between EGFP and mScarlet3 in the 488 and 520 channels was corrected through linear unmixing analysis, as described below. Fluorescence intensity was quantified in ImageJ by measuring the integrated density within equal-area regions of interest for each well. Fluorescence values (EGFP, mScarlet3, and BioTracker) were normalized by the day 0 BioTracker signal measured before transfection to account for variations in starting cell numbers.

Linear unmixing analysis
saRNA constructs encoding individual fluorescent proteins (moxBFP, EGFP, or mScarlet3) were designed to assess cross-excitation among the fluorescent proteins used in this study. tSA201 cells (96121229, ECACC) were seeded in black glass-bottom 6-well plates coated with poly-D-lysine (Sigma) and transfected with the saRNA constructs. Cells were imaged the following day using an Odyssey M laser scanner, with fluorescence captured through the 488 and 520 channels. Expression of moxBFP was undetectable in both the 488 and 520 channels, and therefore it was excluded from further analysis. Bleed-through of EGFP into the 520 channel and mScarlet3 into the 488 channel was quantified using ImageJ, with cross-excitation determined to be 11.32% and 0.94%, respectively.

651 The emission signals were assumed to be linearly proportional to the sum of the intensities
652 of each fluorophore, and the unmixed EGFP and mScarlet3 signals were calculated using
653 Python.
654
655 **Annexin V assay**
656 FLS were stained with BioTracker NIR680 and plated on black glass-bottom 24-well
657 plates (Sensoplate, Greiner Bio-One). Cells were transfected with saRNA or treated with
658 0.5 μM staurosporine (Cayman Chemical) as a positive control.
659 Annexin V-CF800 conjugate (Biotium) was diluted to 250 ng/ml in Live Cell Imaging
660 Solution (Invitrogen). On each day of the assay, wells were washed with Live Cell
661 Imaging Solution and replaced with diluted Annexin V-CF800 solution. Plates were
662 incubated at 37°C for 15 minutes. Following incubation, plates were washed 3 times with
663 Live Cell Imaging Solution before imaging the 700 and 800 channels with an Odyssey M
664 imager set to +1.45 mm image offset and 100 μm resolution.
665 Image analysis was performed using ImageJ. To correct for unidirectional spectral bleed-
666 through of BioTracker NIR680 into the 800-channel, subtractive compensation was
667 applied by dividing the 700-channel image by a factor of 800 and then subtracting it from
668 the 800-channel image. Due to the presence of a small number of high-intensity speckles
669 in the 800-channel image, area rather than fluorescence intensity was quantified. The
670 display range of the 800-channel image was set between 0.25 and 2.5 and the image was
671 thresholded using the method of Li (*85*). The area of thresholded pixels within each well
672 was then quantified and adjusted based on the BioTracker signal before transfection to
673 account for variations in cell numbers. Data was then normalized to the average of the
674 mock transfection condition.
675
676 **Calcein AM staining**
677 Calcein AM (Invitrogen) staining was performed according to the manufacturer's
678 protocol. Briefly, cells were washed with HBSS and incubated with 2 μM calcein AM
679 (diluted in HBSS) at 37°C for 30 minutes. Following three washes, cells were imaged in
680 Live Cell Imaging Solution, and the 488-channel image was captured using an Odyssey M
681 imager.
682 Although calcein AM and EGFP share overlapping spectra, calcein AM fluorescence was
683 typically much higher than EGFP, making EGFP's contribution to the measured Calcein
684 AM signal negligible in most cases. However, when the E3 construct was used, EGFP
685 expression was sufficient to interfere with the signal. To address this, in experiments that
686 included use of the E3 construct, a 488-channel image was captured prior to calcein AM
687 application and subtracted from the post-application image to accurately measure calcein
688 AM fluorescence.
689 Fluorescence intensity was quantified using ImageJ. In experiments where BioTracker
690 was used, fluorescence values were corrected by the pre-transfection BioTracker signal to
691 account for differences in starting cell numbers.
692
693 **In-cell western assay**
694 Cells were plated on black, glass-bottom 24-well plates. Alongside mock and saRNA
695 transfections, one well was reserved for background subtraction, which received no
696 treatment. Unless specified otherwise, experiments were conducted 2 days post-
697 transfection. Cells were fixed with 4% paraformaldehyde for 10 minutes at room
698 temperature, followed by two washes with tris-buffered saline (TBS). Permeabilization
699 was then performed using 0.1% Triton X-100 in TBS for 10 minutes, followed by two

additional TBS washes. After permeabilization, cells were blocked with Intercept TBS Blocking Buffer (LI-COR) for 1 hour at room temperature with gentle agitation. Primary antibodies were diluted in Intercept Blocking Buffer and incubated with the cells overnight at 4°C. The background subtraction well was incubated with blocking buffer alone, without primary antibodies. The following primary antibodies were used: Phospho-eIF2α (Ser51) (D9G8) XP rabbit monoclonal (1:200, #3398, Cell Signaling Technology), eIF2α (L57A5) mouse monoclonal (1:200, #2103, Cell Signaling Technology), PKR rabbit polyclonal (1:500, #18244-1-AP, Proteintech), Phospho-eIF4E (S209) rabbit monoclonal (1:200, #ab76256, Abcam), eIF4E mouse monoclonal (5D11) (1:200, #MA1-089, Invitrogen), and fibroblast activation protein (73.3) mouse monoclonal (20 µg/ml, #BE0374, InVivoMAb). Except for the fibroblast activation protein antibody, which was conjugated to DyLight 800 using the manufacturer's DyLight Antibody Labeling Kit (#53062, Thermo Scientific), all primary antibodies were unconjugated.
After washing the wells three times with TBS, cells were incubated for 1 hour at room temperature with the appropriate secondary antibodies or normalization stain, with gentle agitation. The secondary antibodies used were goat anti-mouse IRDye 800CW (1:800), donkey anti-rabbit IRDye 800CW (1:800), donkey anti-mouse IRDye 680RD (1:800), and CellTag 700 (1:500), all from LI-COR. The background subtraction well received secondary antibody but no CellTag. Following four additional washes with TBS, the plate was inverted and gently tapped on absorbent paper to remove excess liquid. The plate was then imaged using the Odyssey M imager with LI-COR Acquisition software using a plate offset of +1.45 and 100 µm resolution. Signal quantification was carried out using Empiria Studio software (LI-COR).

RNA integrity analysis

FLS were plated in 6-well plates and transfected with either saRNA or subjected to mock transfection. After 26-30 hours, cells were harvested by scraping in 350 µl RLT buffer (QIAGEN) supplemented with 10 µl/ml β-mercaptoethanol (Sigma). Cell lysates were homogenized using QIAshredder columns (QIAGEN), and total RNA was extracted using the RNeasy Mini Kit (QIAGEN) according to the manufacturer's instructions. RNA quantity and quality were initially assessed using a N60 nanophotometer (Implen). Samples were aliquoted and stored at -80°C until further analysis. For detailed quality assessment, samples were transported on dry ice and analyzed using the RNA Pico Kit on the 2100 Bioanalyzer system (Agilent), performed by Cambridge Genomic Services. RNA Integrity Number (RIN) values were determined for each sample, and the differences in RIN between saRNA-transfected and mock-transfected conditions were calculated.

Bead-based immunoassay

FLS were stained with BioTracker and seeded onto 6-well plates. After transfection, the saRNA-lipofectamine complexes were replaced with 2 ml of fresh FLS media. Two days later, supernatants were collected and stored at -80°C until analysis. On the day of analysis, the supernatant was thawed on ice, and levels of 13 innate immune-related cytokines (IFN-γ, CXCL1, TNF-α, MCP-1, IL-12p70, CCL5, IL-1β, CXCL10, GM-CSF, IL-10, IFN-β, IFN-α, and IL-6) were measured using the LEGENDplex Mouse Anti-Virus Response Panel (740621, BioLegend) following the manufacturer's protocol. Samples were run in duplicate. A custom 3D-printed PETG vacuum manifold (designed with Fusion 360) was used for vacuum filtration, and beads were analyzed using a CytoPLEX LX flow cytometer (Beckman Coulter). Data analysis was performed with the LEGENDplex Qognit Data Analysis Suite (BioLegend). To account for differences in cell

numbers between wells, cytokine levels were corrected based on the BioTracker signal before transfection.

ML336 experiments

ML336 (Cayman Chemical) was dissolved in DMSO (Sigma) at a stock concentration of 10 mM, and aliquots were stored at -20°C. For treatments, ML336 was added to cell cultures at a final concentration of 1 μM, while vehicle control cultures received 0.01% DMSO.

Statistical Analysis

All statistical analyses were conducted using GraphPad Prism 9, with specific tests detailed in the corresponding figure legends. All statistical tests were two-sided tests.

References

1. N. Silva-Pilipich, U. Beloki, L. Salaberry, C. Smerdou, Self-Amplifying RNA: A Second Revolution of mRNA Vaccines against COVID-19. *Vaccines (Basel)* **12**, 318 (2024).

2. K. Bloom, F. van den Berg, P. Arbuthnot, Self-amplifying RNA vaccines for infectious diseases. *Gene Ther* **28**, 117–129 (2021).

3. M. K. Pietilä, K. Hellström, T. Ahola, Alphavirus polymerase and RNA replication. *Virus Research* **234**, 44–57 (2017).

4. G. Maruggi, C. Zhang, J. Li, J. B. Ulmer, D. Yu, mRNA as a Transformative Technology for Vaccine Development to Control Infectious Diseases. *Mol Ther* **27**, 757–772 (2019).

5. I. Akhrymuk, I. Frolov, E. I. Frolova, Both RIG-I and MDA5 detect alphavirus replication in concentration-dependent mode. *Virology* **487**, 230–241 (2016).

6. Y. Gong, D. Yong, G. Liu, J. Xu, J. Ding, W. Jia, A Novel Self-Amplifying mRNA with Decreased Cytotoxicity and Enhanced Protein Expression by Macrodomain Mutations. *Advanced Science* **n/a**, 2402936 (2024).

7. R. Gorchakov, E. Frolova, B. R. G. Williams, C. M. Rice, I. Frolov, PKR-Dependent and -Independent Mechanisms Are Involved in Translational Shutoff during Sindbis Virus Infection. *Journal of Virology* **78**, 8455–8467 (2004).

8. F. Dominguez, O. Palchevska, E. I. Frolova, I. Frolov, Alphavirus-based replicons demonstrate different interactions with host cells and can be optimized to increase protein expression. *Journal of Virology* **97**, e01225-23 (2023).

9. H. Vanluchene, O. Gillon, K. Peynshaert, S. C. De Smedt, N. Sanders, K. Raemdonck, K. Remaut, Less is more: Self-amplifying mRNA becomes self-killing upon dose escalation in immune-competent retinal cells. *European Journal of Pharmaceutics and Biopharmaceutics* **196**, 114204 (2024).

10. F. Terenzi, M. J. deVeer, H. Ying, N. P. Restifo, B. R. Williams, R. H. Silverman, The antiviral enzymes PKR and RNase L suppress gene expression from viral and non-viral based vectors. *Nucleic Acids Res* **27**, 4369–4375 (1999).

11. C. Urban, C. Rhême, S. Maerz, B. Berg, R. Pick, R. Nitschke, C. Borner, Apoptosis induced by Semliki Forest virus is RNA replication dependent and mediated via Bak. *Cell Death Differ* **15**, 1396–1407 (2008).

12. T. Pepini, A.-M. Pulichino, T. Carsillo, A. L. Carlson, F. Sari-Sarraf, K. Ramsauer, J. C. Debasitis, G. Maruggi, G. R. Otten, A. J. Geall, D. Yu, J. B. Ulmer, C. Iavarone, Induction of an IFN-Mediated Antiviral Response by a Self-Amplifying RNA Vaccine: Implications for Vaccine Design. *The Journal of Immunology* **198**, 4012–4024 (2017).

794 13. A. K. Blakney, P. F. McKay, C. R. Bouton, K. Hu, K. Samnuan, R. J. Shattock, Innate Inhibiting Proteins
795 Enhance Expression and Immunogenicity of Self-Amplifying RNA. *Mol Ther* **29**, 1174–1185 (2021).

796 14. A. K. Blakney, S. Ip, A. J. Geall, An Update on Self-Amplifying mRNA Vaccine Development. *Vaccines*
797 *(Basel)* **9**, 97 (2021).

798 15. A.-K. Minnaert, H. Vanluchene, R. Verbeke, I. Lentacker, S. C. De Smedt, K. Raemdonck, N. N. Sanders, K.
799 Remaut, Strategies for controlling the innate immune activity of conventional and self-amplifying mRNA
800 therapeutics: Getting the message across. *Adv Drug Deliv Rev* **176**, 113900 (2021).

801 16. J. H. Erasmus, J. Archer, J. Fuerte-Stone, A. P. Khandhar, E. Voigt, B. Granger, R. G. Bombardi, J. Govero, Q.
802 Tan, L. A. Durnell, R. N. Coler, M. S. Diamond, J. E. Crowe, S. G. Reed, L. B. Thackray, R. H. Carnahan, N.
803 V. Hoeven, Intramuscular Delivery of Replicon RNA Encoding ZIKV-117 Human Monoclonal Antibody
804 Protects against Zika Virus Infection. *Molecular Therapy Methods & Clinical Development* **18**, 402–414
805 (2020).

806 17. J. E. McGee, J. R. Kirsch, D. Kenney, F. Cerbo, E. C. Chavez, T.-Y. Shih, F. Douam, W. W. Wong, M. W.
807 Grinstaff, Complete substitution with modified nucleotides in self-amplifying RNA suppresses the interferon
808 response and increases potency. *Nat Biotechnol*, 1–7 (2024).

809 18. T. Beissert, L. Koste, M. Perkovic, K. C. Walzer, S. Erbar, A. Selmi, M. Diken, S. Kreiter, Ö. Türeci, U. Sahin,
810 Improvement of In Vivo Expression of Genes Delivered by Self-Amplifying RNA Using Vaccinia Virus
811 Immune Evasion Proteins. *Hum Gene Ther* **28**, 1138–1146 (2017).

812 19. N. Yoshioka, E. Gros, H.-R. Li, S. Kumar, D. C. Deacon, C. Maron, A. R. Muotri, N. C. Chi, X.-D. Fu, B. D.
813 Yu, S. F. Dowdy, Efficient Generation of Human iPS Cells by a Synthetic Self-Replicative RNA. *Cell Stem*
814 *Cell* **13**, 10.1016/j.stem.2013.06.001 (2013).

815 20. Y. Xue, Y. Zhang, Y. Zhong, S. Du, X. Hou, W. Li, H. Li, S. Wang, C. Wang, J. Yan, D. D. Kang, B. Deng, D.
816 W. McComb, D. J. Irvine, R. Weiss, Y. Dong, LNP-RNA-engineered adipose stem cells for accelerated
817 diabetic wound healing. *Nat Commun* **15**, 739 (2024).

818 21. Y. Li, B. Teague, Y. Zhang, Z. Su, E. Porter, B. Dobosh, T. Wagner, D. J. Irvine, R. Weiss, In vitro evolution
819 of enhanced RNA replicons for immunotherapy. *Sci Rep* **9**, 6932 (2019).

820 22. A. Maglaviceanu, B. Wu, M. Kapoor, Fibroblast-like synoviocytes: Role in synovial fibrosis associated with
821 osteoarthritis. *Wound Repair and Regeneration* **29**, 642–649 (2021).

822 23. M. J. Mousavi, J. Karami, S. Aslani, M. N. Tahmasebi, A. S. Vaziri, A. Jamshidi, E. Farhadi, M. Mahmoudi,
823 Transformation of fibroblast-like synoviocytes in rheumatoid arthritis; from a friend to foe. *Autoimmun*
824 *Highlights* **12**, 3 (2021).

825 24. M. Szczerba, S. Subramanian, K. Trainor, M. McCaughan, K. V. Kibler, B. L. Jacobs, Small Hero with Great
826 Powers: Vaccinia Virus E3 Protein and Evasion of the Type I IFN Response. *Biomedicines* **10**, 235 (2022).

827 25. B. Kalveram, T. Ikegami, Toscana Virus NSs Protein Promotes Degradation of Double-Stranded RNA-
828 Dependent Protein Kinase. *J Virol* **87**, 3710–3718 (2013).

829 26. M. Drappier, B. K. Jha, S. Stone, R. Elliott, R. Zhang, D. Vertommen, S. R. Weiss, R. H. Silverman, T.
830 Michiels, A novel mechanism of RNase L inhibition: Theiler's virus L* protein prevents 2-5A from binding to
831 RNase L. *PLoS Pathog* **14**, e1006989 (2018).

832 27. J.-C. Mars, B. Culjkovic-Kraljacic, K. L. B. Borden, eIF4E orchestrates mRNA processing, RNA export and
833 translation to modify specific protein production. *Nucleus* **15**, 2360196 (2024).

834 28. M. G. Santoro, A. Rossi, C. Amici, NF-κB and virus infection: who controls whom. *The EMBO Journal* **22**,
835 2552–2560 (2003).

836 29. J. P. Mitchell, R. J. Carmody, "Chapter Two - NF-κB and the Transcriptional Control of Inflammation" in
837 *International Review of Cell and Molecular Biology*, F. Loos, Ed. (Academic Press, 2018;

838 https://www.sciencedirect.com/science/article/pii/S1937644817300825)vol. 335 of *Transcriptional Gene*
839 *Regulation in Health and Disease*, pp. 41–84.

840 30. Y.-R. Lee, S.-H. Kweon, K.-B. Kwon, J.-W. Park, T.-R. Yoon, B.-H. Park, Inhibition of IL-1β-mediated
841 inflammatory responses by the IκBα super-repressor in human fibroblast-like synoviocytes. *Biochemical and*
842 *Biophysical Research Communications* **378**, 90–94 (2009).

843 31. K. Brown, S. Gerstberger, L. Carlson, G. Franzoso, U. Siebenlist, Control of IκB-α Proteolysis by Site-
844 Specific, Signal-Induced Phosphorylation. *Science* **267**, 1485–1488 (1995).

845 32. X. Yan, Z. Liu, Y. Chen, Regulation of TGF-β signaling by Smad7. *Acta Biochimica et Biophysica Sinica* **41**,
846 263–272 (2009).

847 33. M. L. Sobah, C. Liongue, A. C. Ward, SOCS Proteins in Immunity, Inflammatory Diseases, and Immune-
848 Related Cancer. *Front Med (Lausanne)* **8**, 727987 (2021).

849 34. I. D. Dimitriou, L. Clemenza, A. J. Scotter, G. Chen, F. M. Guerra, R. Rottapel, Putting out the fire:
850 coordinated suppression of the innate and adaptive immune systems by SOCS1 and SOCS3 proteins.
851 *Immunological Reviews* **224**, 265–283 (2008).

852 35. T. Blumer, M. Coto-Llerena, F. H. T. Duong, M. H. Heim, SOCS1 is an inducible negative regulator of
853 interferon λ (IFN-λ)-induced gene expression in vivo. *J Biol Chem* **292**, 17928–17938 (2017).

854 36. Z. Liu, O. Chen, J. B. J. Wall, M. Zheng, Y. Zhou, L. Wang, H. Ruth Vaseghi, L. Qian, J. Liu, Systematic
855 comparison of 2A peptides for cloning multi-genes in a polycistronic vector. *Sci Rep* **7**, 2193 (2017).

856 37. A.-C. Gingras, B. Raught, N. Sonenberg, eIF4 Initiation Factors: Effectors of mRNA Recruitment to
857 Ribosomes and Regulators of Translation. *Annu. Rev. Biochem.* **68**, 913–963 (1999).

858 38. D. Chung, C. E. Schroeder, J. Sotsky, T. Yao, S. Roy, R. A. Smith, N. A. Tower, J. W. Noah, S. McKellip, M.
859 Sosa, L. Rasmussen, E. L. White, J. Aubé, J. E. Golden, "ML336: Development of Quinazolinone-Based
860 Inhibitors Against Venezuelan Equine Encephalitis Virus (VEEV)" in *Probe Reports from the NIH Molecular*
861 *Libraries Program* (National Center for Biotechnology Information (US), Bethesda (MD), 2010;
862 http://www.ncbi.nlm.nih.gov/books/NBK179829/).

863 39. D. F. Boyd, E. K. Allen, A. G. Randolph, X. J. Guo, Y. Weng, C. J. Sanders, R. Bajracharya, N. K. Lee, C. S.
864 Guy, P. Vogel, W. Guan, Y. Li, X. Liu, T. Novak, M. M. Newhams, T. P. Fabrizio, N. Wohlgemuth, P. M.
865 Mourani, T. N. Wight, S. Schultz-Cherry, S. A. Cormier, K. Shaw-Saliba, A. Pekosz, R. E. Rothman, K.-F.
866 Chen, Z. Yang, R. J. Webby, N. Zhong, J. C. Crawford, P. G. Thomas, Exuberant fibroblast activity
867 compromises lung function via ADAMTS-4. *Nature* **587**, 466–471 (2020).

868 40. T. Krausgruber, N. Fortelny, V. Fife-Gernedl, M. Senekowitsch, L. C. Schuster, A. Lercher, A. Nemc, C.
869 Schmidl, A. F. Rendeiro, A. Bergthaler, C. Bock, Structural cells are key regulators of organ-specific immune
870 response. *Nature* **583**, 296–302 (2020).

871 41. A. P. Croft, J. Campos, K. Jansen, J. D. Turner, J. Marshall, M. Attar, L. Savary, C. Wehmeyer, A. J. Naylor,
872 S. Kemble, J. Begum, K. Duerholz, H. Perlman, F. Barone, H. M. McGettrick, D. T. Fearon, K. Wei, S.
873 Raychaudhuri, I. Korsunsky, M. B. Brenner, M. Coles, S. N. Sansom, A. Filer, C. D. Buckley, Distinct
874 fibroblast subsets drive inflammation and damage in arthritis. *Nature* **570**, 246–251 (2019).

875 42. S. Bauer, M. C. Jendro, A. Wadle, S. Kleber, F. Stenner, R. Dinser, A. Reich, E. Faccin, S. Gödde, H. Dinges,
876 U. Müller-Ladner, C. Renner, Fibroblast activation protein is expressed by rheumatoid myofibroblast-like
877 synoviocytes. *Arthritis Res Ther* **8**, R171 (2006).

878 43. H. E. Zhang, E. J. Hamson, M. M. Koczorowska, S. Tholen, S. Chowdhury, C. G. Bailey, A. J. Lay, S. M.
879 Twigg, Q. Lee, B. Roediger, M. L. Biniossek, M. B. O'Rourke, G. W. McCaughan, F. M. Keane, O. Schilling,
880 M. D. Gorrell, Identification of Novel Natural Substrates of Fibroblast Activation Protein-alpha by Differential
881 Degradomics and Proteomics. *Mol Cell Proteomics* **18**, 65–85 (2019).

882 44. S. Wäldele, C. Koers-Wunrau, D. Beckmann, A. Korb-Pap, C. Wehmeyer, T. Pap, B. Dankbar, Deficiency of
883 fibroblast activation protein alpha ameliorates cartilage destruction in inflammatory destructive arthritis.
884 *Arthritis Res Ther* **17**, 12 (2015).

885 45. J. S. Tregoning, D. C. Stirling, Z. Wang, K. E. Flight, J. C. Brown, A. K. Blakney, P. F. McKay, R. F. Cunliffe,
886 V. Murugaiah, C. B. Fox, M. Beattie, Y. K. Tam, C. Johansson, R. J. Shattock, Formulation, inflammation, and
887 RNA sensing impact the immunogenicity of self-amplifying RNA vaccines. *Molecular Therapy Nucleic Acids*
888 **31**, 29–42 (2023).

889 46. N. V. Bathula, J. J. Friesen, I. C. Casmil, C. J. Wayne, S. Liao, S. K. V. Soriano, C. H. Ho, A. Strumpel, A. K.
890 Blakney, Delivery vehicle and route of administration influences self-amplifying RNA biodistribution,
891 expression kinetics, and reactogenicity. *Journal of Controlled Release* **374**, 28–38 (2024).

892 47. Y. Oda, Y. Kumagai, M. Kanai, Y. Iwama, I. Okura, T. Minamida, Y. Yagi, T. Kurosawa, B. Greener, Y.
893 Zhang, J. L. Walson, Immunogenicity and safety of a booster dose of a self-amplifying RNA COVID-19
894 vaccine (ARCT-154) versus BNT162b2 mRNA COVID-19 vaccine: a double-blind, multicentre, randomised,
895 controlled, phase 3, non-inferiority trial. *The Lancet Infectious Diseases* **24**, 351–360 (2024).

896 48. A. Saraf, R. Gurjar, S. Kaviraj, A. Kulkarni, D. Kumar, R. Kulkarni, R. Virkar, J. Krishnan, A. Yadav, E.
897 Baranwal, A. Singh, A. Raghuwanshi, P. Agarwal, L. Savergave, S. Singh, GEMCOVAC-OM Study
898 Investigators, An Omicron-specific, self-amplifying mRNA booster vaccine for COVID-19: a phase 2/3
899 randomized trial. *Nat Med* **30**, 1363–1372 (2024).

900 49. S. Atasheva, V. Krendelchtchikova, A. Liopo, E. Frolova, I. Frolov, Interplay of Acute and Persistent
901 Infections Caused by Venezuelan Equine Encephalitis Virus Encoding Mutated Capsid Protein. *Journal of*
902 *Virology* **84**, 10004–10015 (2010).

903 50. A. Koch, L. Aguilera, T. Morisaki, B. Munsky, T. J. Stasevich, Quantifying the dynamics of IRES and cap
904 translation with single-molecule resolution in live cells. *Nat Struct Mol Biol* **27**, 1095–1104 (2020).

905 51. P. Berglund, D. Finzi, J. R. Bennink, J. W. Yewdell, Viral Alteration of Cellular Translational Machinery
906 Increases Defective Ribosomal Products. *Journal of Virology* **81**, 7220–7229 (2007).

907 52. J. J. Fros, G. P. Pijlman, Alphavirus Infection: Host Cell Shut-Off and Inhibition of Antiviral Responses.
908 *Viruses* **8**, 166 (2016).

909 53. Y. V. Svitkin, B. Herdy, M. Costa-Mattioli, A.-C. Gingras, B. Raught, N. Sonenberg, Eukaryotic translation
910 initiation factor 4E availability controls the switch between cap-dependent and internal ribosomal entry site-
911 mediated translation. *Mol Cell Biol* **25**, 10556–10565 (2005).

912 54. C. Chang, N. Music, M. Cheung, E. Rossignol, S. Bedi, H. Patel, M. Safari, C. Lee, G. R. Otten, E. C.
913 Settembre, G. Palladino, Y. Wen, Self-amplifying mRNA bicistronic influenza vaccines raise cross-reactive
914 immune responses in mice and prevent infection in ferrets. *Molecular Therapy Methods & Clinical*
915 *Development* **27**, 195–205 (2022).

916 55. F. Hariri, M. Arguello, L. Volpon, B. Culjkovic-Kraljacic, T. H. Nielsen, J. Hiscott, K. K. Mann, K. L. B.
917 Borden, The eukaryotic translation initiation factor eIF4E is a direct transcriptional target of NF-κB and is
918 aberrantly regulated in acute myeloid leukemia. *Leukemia* **27**, 2047–2055 (2013).

919 56. S. Uttam, C. Wong, T. J. Price, A. Khoutorsky, eIF4E-Dependent Translational Control: A Central Mechanism
920 for Regulation of Pain Plasticity. *Front Genet* **9**, 470 (2018).

921 57. N. Siddiqui, N. Sonenberg, Signalling to eIF4E in cancer. *Biochemical Society Transactions* **43**, 763–772
922 (2015).

923 58. C. G. Gkogkas, A. Khoutorsky, I. Ran, E. Rampakakis, T. Nevarko, D. B. Weatherill, C. Vasuta, S. Yee, M.
924 Truitt, P. Dallaire, F. Major, P. Lasko, D. Ruggero, K. Nader, J.-C. Lacaille, N. Sonenberg, Autism-related
925 deficits via dysregulated eIF4E-dependent translational control. *Nature* **493**, 371–377 (2013).

926 59. P. Syntichaki, K. Troulinaki, N. Tavernarakis, eIF4E function in somatic cells modulates ageing in
927 Caenorhabditis elegans. *Nature* **445**, 922–926 (2007).

928 60. M. Costa-Mattioli, P. Walter, The integrated stress response: From mechanism to disease. *Science* **368**,
929 eaat5314 (2020).

930 61. T. Liu, L. Zhang, D. Joo, S.-C. Sun, NF-κB signaling in inflammation. *Sig Transduct Target Ther* **2**, 1–9
931 (2017).

932 62. J.-L. Luo, H. Kamata,, M. Karin, IKK/NF-κB signaling: balancing life and death – a new approach to cancer
933 therapy. *Journal of Clinical Investigation* **115**, 2625–2632 (2005).

934 63. A. V. Miagkov, D. V. Kovalenko, C. E. Brown, J. R. Didsbury, J. P. Cogswell, S. A. Stimpson, A. S. Baldwin,
935 S. S. Makarov, NF-κB activation provides the potential link between inflammation and hyperplasia in the
936 arthritic joint. *Proceedings of the National Academy of Sciences* **95**, 13859–13864 (1998).

937 64. H. G. Zhang, N. Huang, D. Liu, L. Bilbao, X. Zhang, P. Yang, T. Zhou, D. T. Curiel, J. D. Mountz, Gene
938 therapy that inhibits nuclear translocation of nuclear factor kappaB results in tumor necrosis factor alpha-
939 induced apoptosis of human synovial fibroblasts. *Arthritis Rheum* **43**, 1094–1105 (2000).

940 65. Y. Yamamura, X. Hua, S. Bergelson, H. F. Lodish, Critical Role of Smads and AP-1 Complex in Transforming
941 Growth Factor-β-dependent Apoptosis. *Journal of Biological Chemistry* **275**, 36295–36302 (2000).

942 66. S. Patil, G. M. Wildey, T. L. Brown, L. Choy, R. Derynck, P. H. Howe, Smad7 is induced by CD40 and
943 protects WEHI 231 B-lymphocytes from transforming growth factor-beta -induced growth inhibition and
944 apoptosis. *J Biol Chem* **275**, 38363–38370 (2000).

945 67. K. Zitzmann, S. Brand, E. N. De Toni, S. Baehs, B. Göke, J. Meinecke, G. Spöttl, H. H. H. D. Meyer, C. J.
946 Auernhammer, SOCS1 Silencing Enhances Antitumor Activity of Type I IFNs by Regulating Apoptosis in
947 Neuroendocrine Tumor Cells. *Cancer Research* **67**, 5025–5032 (2007).

948 68. M. N. Mann-Chandler, M. Kashyap, H. V. Wright, F. Norozian, B. O. Barnstein, S. Gingras, E. Parganas, J. J.
949 Ryan, IFN-γ Induces Apoptosis in Developing Mast Cells1. *The Journal of Immunology* **175**, 3000–3005
950 (2005).

951 69. A. Kimura, T. Naka, S. Nagata, I. Kawase, T. Kishimoto, SOCS-1 suppresses TNF-alpha-induced apoptosis
952 through the regulation of Jak activation. *Int Immunol* **16**, 991–999 (2004).

953 70. S. Madonna, C. Scarponi, S. Pallotta, A. Cavani, C. Albanesi, Anti-apoptotic effects of suppressor of cytokine
954 signaling 3 and 1 in psoriasis. *Cell Death Dis* **3**, e334–e334 (2012).

955 71. L. Yan, Q. Tang, D. Shen, S. Peng, Q. Zheng, H. Guo, M. Jiang, W. Deng, SOCS-1 Inhibits TNF-α-Induced
956 Cardiomyocyte Apoptosis via ERK1/2 Pathway Activation. *Inflammation* **31**, 180–188 (2008).

957 72. B. Goker Bagca, C. Biray Avci, The potential of JAK/STAT pathway inhibition by ruxolitinib in the treatment
958 of COVID-19. *Cytokine & Growth Factor Reviews* **54**, 51–61 (2020).

959 73. N. P. D. Liau, A. Laktyushin, I. S. Lucet, J. M. Murphy, S. Yao, E. Whitlock, K. Callaghan, N. A. Nicola, N. J.
960 Kershaw, J. J. Babon, The molecular basis of JAK/STAT inhibition by SOCS1. *Nat Commun* **9**, 1558 (2018).

961 74. J. A. Roman-Blas, S. A. Jimenez, NF-κB as a potential therapeutic target in osteoarthritis and rheumatoid
962 arthritis. *Osteoarthritis and Cartilage* **14**, 839–848 (2006).

963 75. J. Shen, S. Li, D. Chen, TGF-β signaling and the development of osteoarthritis. *Bone Res* **2**, 1–7 (2014).

964 76. Q. Zhou, Q. Ren, L. Jiao, J. Huang, J. Yi, J. Chen, J. Lai, G. Ji, T. Zheng, The potential roles of JAK/STAT
965 signaling in the progression of osteoarthritis. *Front. Endocrinol.* **13** (2022).

77. N. M. Blackwell, P. Sembi, J. S. Newson, T. Lawrence, D. W. Gilroy, P. S. Kabouridis, Reduced infiltration and increased apoptosis of leukocytes at sites of inflammation by systemic administration of a membrane-permeable IκBα repressor. *Arthritis & Rheumatism* **50**, 2675–2684 (2004).

78. S.-Y. Chen, A.-L. Shiau, C.-L. Wu, C.-R. Wang, Intraarticular overexpression of Smad7 ameliorates experimental arthritis. *Sci Rep* **6**, 35163 (2016).

79. Y.-J. Ha, Y. S. Choi, E. H. Kang, K. Shin, T. K. Kim, Y. W. Song, Y. J. Lee, SOCS1 suppresses IL-1β-induced C/EBPβ expression via transcriptional regulation in human chondrocytes. *Exp Mol Med* **48**, e241–e241 (2016).

80. A. M. Skidmore, R. S. Adcock, C. B. Jonsson, J. E. Golden, D.-H. Chung, Benzamidine ML336 inhibits plus and minus strand RNA synthesis of Venezuelan equine encephalitis virus without affecting host RNA production. *Antiviral Research* **174**, 104674 (2020).

81. C. E. Schroeder, T. Yao, J. Sotsky, R. A. Smith, S. Roy, Y.-K. Chu, H. Guo, N. A. Tower, J. W. Noah, S. McKellip, M. Sosa, L. Rasmussen, L. H. Smith, E. L. White, J. Aubé, C. B. Jonsson, D. Chung, J. E. Golden, Development of (E)-2-((1,4-Dimethylpiperazin-2-ylidene)amino)-5-nitro-N-phenylbenzamide, ML336: Novel 2-Amidinophenylbenzamides as Potent Inhibitors of Venezuelan Equine Encephalitis Virus. *J. Med. Chem.* **57**, 8608–8621 (2014).

82. T. W. J. Gadella, L. van Weeren, J. Stouthamer, M. A. Hink, A. H. G. Wolters, B. N. G. Giepmans, S. Aumonier, J. Dupuy, A. Royant, mScarlet3: a brilliant and fast-maturing red fluorescent protein. *Nat Methods* **20**, 541–545 (2023).

83. L. M. Costantini, M. Baloban, M. L. Markwardt, M. A. Rizzo, F. Guo, V. V. Verkhusha, E. L. Snapp, A palette of fluorescent proteins optimized for diverse cellular environments. *Nat Commun* **6**, 7670 (2015).

84. S. Chakrabarti, Z. Hore, L. A. Pattison, S. Lalnunhlimi, C. N. Bhebhe, G. Callejo, D. C. Bulmer, L. S. Taams, F. Denk, E. S. J. Smith, Sensitization of knee-innervating sensory neurons by tumor necrosis factor-α-activated fibroblast-like synoviocytes: an in vitro, coculture model of inflammatory pain. *Pain* **161**, 2129–2141 (2020).

85. C. H. Li, C. K. Lee, Minimum cross entropy thresholding. *Pattern Recognition* **26**, 617–625 (1993).

Acknowledgments

The authors gratefully acknowledge the Cambridge Advanced Imaging Centre, the flow cytometry facility from the School of the Biological Sciences, and Cambridge Genomic Services for their support & assistance in this work. The authors would like to thank Dr. Paul Miller for providing the pDx_mScarlet3 plasmid and Dr. Alex Cloake for providing the pIRES2-EGFP plasmid used in this study.

Funding:
Marie Skłodowska-Curie Actions Postdoctoral Fellowship—UKRI guarantee EP/X023117/1 (TKL)
AstraZeneca PhD studentship G115018 (AR)
AstraZeneca PhD studentship G113502 (LWP)
MRC Postdoctoral Training Scheme (LF)
MICA ADVANTAGE visceral pain consortium: Advanced Discovery of Visceral Analgesics via Neuroimmune Targets and the Genetics of Extreme human phenotype MR/W002426/1 (EStJS)
Wellcome Trust 225856/Z/22/Z (EStJS)

Author contributions:

Conceptualization: TKL, EStJS
Formal analysis: TKL, EStJS
Funding acquisition: EStJS, TKL
Investigation: TKL, AR, LWP
Methodology: TKL, TA
Resources: EStJS, TKL
Software: LF
Supervision: EStJS, TKL
Visualisation: TKL, EStJS
Writing—original draft: TKL
Writing—reviewing & editing: EStJS

Competing interests: Authors declare that they have no competing interests.

Data and materials availability:

The 3D printed vacuum manifold compatible with the LEGENDplex assay has been deposited in the NIH 3D print exchange (3DPX-021388).

All data needed to evaluate the conclusions in the paper are present in the paper, the Supplementary Materials, and the Figshare repository. Additional data can be accessed at 10.6084/m9.figshare.27091972.